

# Extension of the Generic Multi-Frequency Modelling Method for Type 3 Wind Turbines

**Nouri, Behnam; Kocewiak, Lukasz; Shah, Shahil; Koralewicz, Przemyslaw; Gevorgian, Vahan; Sørensen, Poul**

*Published in:*
IEEE Transactions on Energy Conversion

*Link to article, DOI:*
10.1109/TEC.2022.3166470

*Publication date:*
2022

*Document Version*
Peer reviewed version

# Extension of the Generic Multi-Frequency Modelling Method for Type 3 Wind Turbines

Behnam Nouri, *Member, IEEE,* Łukasz Kocewiak, *Senior Member, IEEE,* Shahil Shah, *Senior Member, IEEE,* Przemyslaw Koralewicz, *Member, IEEE,* Vahan Gevorgian, *Senior Member, IEEE,* and Poul Sørensen, *Fellow, IEEE,*

***Abstract*—Reflecting potential non-linearities of converter-based systems, especially frequency and sequence couplings, is an ongoing challenge for linearized multi-frequency models. Besides, design details are required to develop such models, which either are the intellectual property of manufacturers or require experimental tests. The generic multi-frequency modelling method has been proposed to fill this gap; however, it is only developed for converter-connected systems, e.g., Type 4 Wind Turbines (WT). This paper proposes to extend the application of the generic multi-frequency modelling method for Type 3 WTs. In this way, a theory for patterns of the couplings in Type 3 WTs is proposed. Accordingly, a group of emissions and couplings are Rotor-Speed-Dependent (RSD). The RSD emissions and couplings are particular characteristics of Type 3 WTs, which should be addressed in the generic multi-frequency models. The proposed theory is verified by unique-worldwide experimental perturbation tests on a 2 MVA Type 3 WT using a 7 MVA grid emulator. Accordingly, a limited number of RSD couplings and emissions are observed in the test results, mainly in low frequencies (below 1 kHz). Therefore, addressing the RSD couplings is practical and important to extend the generic multi-frequency modelling for Type 3 WTs.**

***Index Terms*—Generic multi-frequency modelling, Frequency couplings, Perturbation test, Type 3 WTs.**

NOMENCLATURE

| | |
|---|---|
| DFT | Discrete Fourier Transform |
| GSC | Grid-Side Converter |
| MFC | Mirror Frequency Coupling |
| PV | Photo-Voltaic |
| POC | Point Of Connection |
| PLL | Phase-Locked-Loop |
| PI | Proportional-Integral |
| PWM | Pulse-Width Modulation |
| RSC | Rotor-Side Converter |
| RSD | Rotor-Speed Dependent |
| WT | Wind Turbine |

## I. Introduction

MULTI-FREQUENCY (or harmonic) interaction is an increasing challenge for power systems due to more and more penetration of converter-based systems, mainly HVDC systems, Wind Turbines (WT), and Photo-Voltaic (PV) converters [1]-[5]. Particularly, interactions and resonances of Type 3 WTs with series-compensated, weak grids and HVDC systems have been reported frequently [4]-[6].

To conduct harmonic stability studies on wind farms consisting Type 3 WTs, averaged multi-frequency models are introduced and developed [6]-[13]. This way, there have been effective attempts to develop analytical multi-frequency models for Type 3 WTs to address the main root causes of non-linearities such as Phase-Locked-Loop (PLL), DC-link dynamics, rotor slip, and frequency and sequence couplings [6]-[12]. However, such models are linearized representatives and vast design information is required to conduct accurate harmonic studies at the system level. Besides, electrical and control design details are the intellectual property of manufacturers and even could be achieved only by experimental tests. Therefore, it is crucial to develop empirical harmonic models to be communicated among different industrial partners for system-level studies.

Recently, we have proposed the generic multi-frequency modelling method for converter-based systems to address the non-linearities by adopting Fourier analysis on responses against perturbation tests in [14]. This way, main couplings, and non-linearities can be identified and addressed in general forms of "$\pm mf_i \pm kf_0$" (k=0,1,2,..., and m=0,1,2,...). The generic multi-frequency model as a Norton equivalent in sequence-domain form can be illustrated as [14]:

$$I_{p(f_i+f_0)} = I_{p0(f_i+f_0)} + \sum_{j=1}^{k} Y_{pp(f_i,f_j)} V_{p(f_j+f_0)} + \sum_{j=1}^{k} Y_{pn(f_i,f_j)} V_{n(f_j-f_0)} \quad (1)$$

$$I_{n(f_i-f_0)} = I_{n0(f_i-f_0)} + \sum_{j=1}^{k} Y_{np(f_i,f_j)} V_{p(f_j+f_0)} + \sum_{j=1}^{k} Y_{nn(f_i,f_j)} V_{n(f_j-f_0)} \quad (2)$$

where $f_0$ refers to the fundamental frequency. The positive sequence currents and voltages are derived from positive sequence perturbations at "$f_i + f_0$" and the negative sequence components are calculated from negative sequence perturbations at "$f_i - f_0$" [9]-[10], [14]. Besides, in [15], a test

B. Nouri (beno@dtu.dk) and P. Sørensen are with the Department of DTU Wind Energy, Technical University of Denmark, 4000 Roskilde, Denmark.

Ł. Kocewiak is with the Ørsted, Nesa Allé 1, 2820 Gentofte, Denmark.

S. Shah, P. Koralewicz and V. Gevorgian are with National Renewable Energy Laboratory (NREL), CO, Golden, USA.

This work has received funding from the European Union's Horizon 2020 research and innovation program under grant agreement No. 691714.

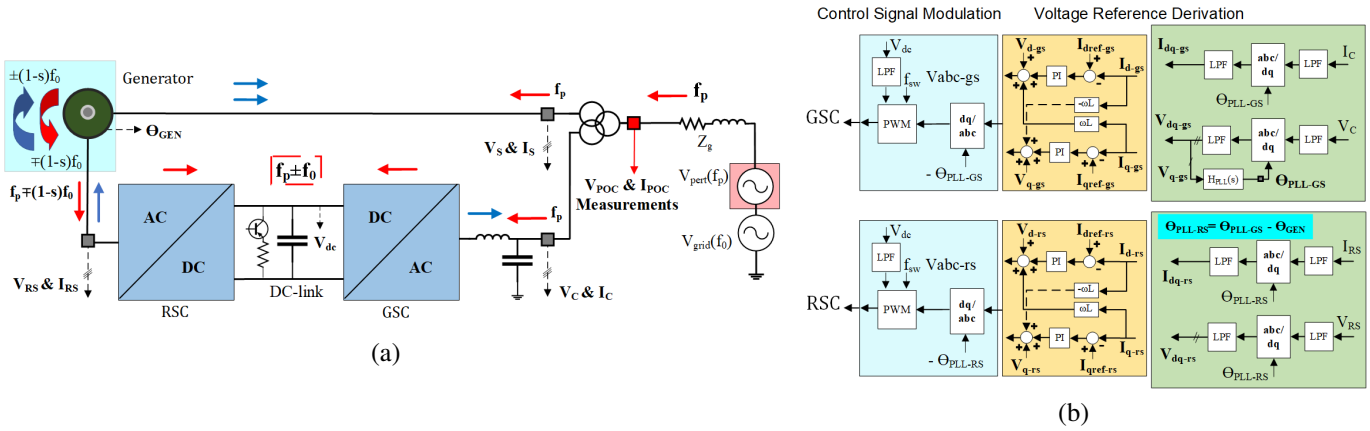


Fig. 1: Schematic diagram of a Type 3 WT (a) with a dq-frame control system (b) in connection to a perturbation source.

methodology along with technical specifications is proposed for the generic multi-frequency modelling using small-signal perturbations.

However, the generic multi-frequency modelling method has been only developed for converter-connected systems (i.e., Type 4 WTs and PV inverters). Therefore, the specific structure of Type 3 WTs with double grid connections through Grid-Side Converter (GSC) and stator of the generator, as illustrated in Fig 1-(a), has been overlooked in the generic multi-frequency modelling method.

The origins of emissions and characteristic harmonics in Type 3 WTs have been studied in [16]-[18]. In [18], the emission patterns in different parts of a Type 3 WT have been formulated in sequence-domain and demonstrated with extensive experiments from different parts of a full-scale Type 3 WT. A group of Rotor-Speed-Dependent (RSD) emissions can be originated by non-ideal generator winding and Rotor-Side Converter (RSC) switching, and emerge in different parts of a Type 3 WT including stator side, rotor side, and DC-link [16]-[18].

The hypothesis of this paper is that RSD emissions can generate RSD couplings in response to perturbations. Identification of the RSD couplings can improve the generic multi-frequency modelling and harmonic stability studies for Type 3 WTs. In this way, a theory for frequency couplings in a typical example of Type 3 WTs is proposed in Part II. The generic multi-frequency modelling method in (1) is extended for Type 3 WTs by including the RSD couplings and emissions in Part III. The unique experimental verification of the proposed theory is demonstrated for a 2MVA Type 3 WT in Part IV.

## II. Rotor-Speed-Dependent Coupling Patterns in Type 3 WTs

In three-phase converter systems with fundamental frequency of $f_0$, the interaction of $f_{dc}$ component in the DC-link voltage with $f_{hr}$ component in the modulation reference can generate the base-band frequency couplings as [14], [19]:

$$f_{dc} \circledast f_{hr} = \{f_{hr}, f_0, f_{hr} \pm f_{dc}, f_0 \pm f_{dc}\} \tag{3}$$

where the sign "$\circledast$" depicts the convolution operation of modulation. Accordingly, four new frequency components can be generated as $\{f_{hr} \pm f_{dc},\ f_0 \pm f_{dc}\}$ which are called "frequency couplings". The concept of frequency coupling generation in (3) can be used to identify the coupling patterns in Type 3 WTs as well.

A typical example of a Type 3 WT structure along with dq-frame control systems for Grid-Side Converter (GSC) and Rotor-Side Converter (RSC) is illustrated in Fig. 1. The coupling principle in (3) can be used for the frequency couplings generated by the GSC. However, for the RSC side, the fundamental frequency should be considered as "$sf_0$". Therefore, the formulation of the couplings at the RSC side can be depicted as:

$$f_{dc} \circledast f_{hr}^r = \{f_{hr}^r, sf_0, f_{hr}^r \pm f_{dc}, sf_0 \pm f_{dc}\} \tag{4}$$

where $f_{hr}^r$ represents the frequency components in the reference signal for RSC.

This way, the frequency couplings in a Type 3 WT can be formulated as a combination of couplings resulting from GSC and RSC using (3)-(4). Considering a small-signal perturbation at the Point Of Connection (POC), the interactions and resulting couplings can be explained as follows:

### A. Frequency components in DC-link

In a Type 3 WT, the characteristic frequency components in DC-link voltage ($f_{dc(ch)}$) are as follows [16]-[18]:

$$f_{dc(ch)} = \{6k(1-s)f_0, mf_{swg} \pm nf_0, mf_{swr} \pm nsf_0\} \tag{5}$$

$$s = \frac{f_0 - pf_m}{f_0} \tag{6}$$

where k,m,n=1,2,..., and $f_{swg}$ and $f_{swr}$ are the switching frequencies of GSC and RSC, respectively. $s$ refers to the rotor slip, $f_m$ is the frequency of the mechanical speed and $p$ is the number of pole pairs. Accordingly, the characteristic frequency components in DC-link originated by MMF

emissions, GSC harmonics (with fundamental frequency of $f_0$) and RSC harmonics (with fundamental frequency of $sf_0$), respectively. Note that in a balanced three-phase system, the coefficients "m,n" are multiples of 6 (i.e., 6, 12, 18, etc) [16]-[18]. Furthermore, as indicated in Fig. 1-(a), positive or negative sequence perturbations with frequency of $f_p$ can flow into the DC-link and originate small-signal frequency components ($f_{dc(ss)}$) as [18]-[19]:

$$f_{dc(ss)} = \{f_p \mp f_0\} \tag{7}$$

where the "-" sign is for positive sequence perturbation and the sign "+" is valid for negative sequence perturbation [18]-[19]. Depending on the bandwidth of electrical and digital filtering in the converters, the frequency components can be observed in a frequency range and can be eliminated in high frequencies.

### *B. Frequency components in control reference*

As it is shown in Fig. 1, a small-signal perturbation at POC (i.e., $f_p$) can flow into the converters' control system through the voltage and current feedback signals, and interfere with the different parts such as reference frame transformations, PLL, Proportional-Integral (PI) control blocks, limiters and Pulse-Width Modulation (PWM) operation [17]-[20]. Such effects can reshape the equivalent impedance of converters and generate couplings at the AC side [17]-[20]. At the first stage, the small-signal perturbation can be presented in the control reference signals of RSC and GSC mainly with the same frequency (i.e., $f_p$) [17]-[18], [20].

### *C. Frequency couplings patterns*

Modulation of the DC-link components in (5) and (7) with the perturbation signal in the control reference can generate couplings at the GSC and RSC sides. The frequency couplings can be categorized as couplings with characteristic harmonics ($F_{ch}$) and small-signal couplings ($F_{ss}$). Therefore, the first group of couplings originated by GSC can be expressed using (5) and (7) as $f_{dc}$ in (3):

$$\begin{aligned} F_{ch(gsc)1} = \{&f_p \pm f_{dc(ch)}, f_0 \pm f_{dc(ch)}\} = \\ \{&f_p \pm [6k(1-s)f_0], f_p \pm (mf_{swg} \pm nf_0), \\ &f_p \pm (mf_{swr} \pm nsf_0), [1 \pm 6k(1-s)]f_0], \\ ,&(n+1)f_0 \pm mf_{swg}, (ns+1)f_0 \pm mf_{swr}\} \end{aligned} \tag{8}$$

$$F_{ss(gsc)1} = \{2f_p \pm f_0, 2f_0 \pm f_p\} \tag{9}$$

Note that the patterns including rotor slip ($s$) express the RSD couplings at the GSC side.

Similar patterns can be formulated for the RSC side. Note that the fundamental frequency for the RSC side should be considered as "$sf_0$". Besides, as shown in Fig. 1-(a), the perturbation at the stator side ($f_p$) is induced to the RSC side with a frequency shift as "$f^r_{hr} = f_p \mp (1-s)f_0$", where the "-" sign is for positive sequence perturbation, and "+" sign is for negative sequence perturbation [16]-[18]. Accordingly, the frequency couplings of RSC in the rotor side can be achieved using (5) and (7) as $f_{dc}$ in (4):

$$\begin{aligned} F^r_{ch(rsc)1} = \{&f_p \mp (1-s)f_0 \pm f_{dc(ch)}, sf_0 \pm f_{dc(ch)}\} = \\ \{&f_p \pm (7k[1-s]f_0), f_p \pm (mf_{swg} \pm [n+1-s]f_0), \\ &f_p \pm (mf_{swr} \pm [(n-1)s+1]f_0), (s \pm 6k[1-s])f_0, \\ &(n+s)f_0 \pm mf_{swg}, (n+1)sf_0 \pm mf_{swr}\} \end{aligned} \tag{10}$$

$$F^r_{ss(rsc)1} = \{2f_p \pm (2-s)f_0, 2f_0 \pm f_p\} \tag{11}$$

Furthermore, the RSC couplings can be induced back to the stator side through the air-gap with "$\pm(1-s)f_0$" frequency shifts [16]-[18]. Therefore, the couplings resulting from RSC at the stator side can be depicted as:

$$\begin{aligned} F^s_{ch(rsc)1} = \{&F^r_{ch(rsc)1} \pm (1-s)f_0\} = \\ \{&f_p \pm (6k[1-s]f_0), f_p \pm (mf_{swg} \pm nf_0), \\ &f_p \pm (mf_{swr} \pm nsf_0), (1 \pm 6k[1-s])f_0, \\ ,&(n+1)f_0 \pm mf_{swg}, (ns+1)f_0 \pm mf_{swr}\} \end{aligned} \tag{12}$$

$$F^s_{ss(rsc)1} = \{2f_p \pm sf_0, 2f_0 \pm f_p\} \tag{13}$$

where $F^s_{ch(rsc)1}$ refers to the couplings with characteristic harmonics and $F^s_{ss(rsc)1}$ refers to the small-signal couplings induced from RSC to the stator side. Note that the patterns in (12)-(13) are similar to the patterns in (8)-(9). Therefore, the GSC and RSC coupling patterns are similar at the stator side of the WT.

### *D. Repetitive generation of couplings*

In the next stage, the newly produced couplings can flow into the control system again in a repetitive loop [14], [20]. The production of the new couplings can be a repetitive process with the interaction of couplings in one stage to generate new patterns in the next stage as explained extensively in [14], [20]. The repetitive production of couplings is limited to the power of the first stage perturbation and any potential amplification by the converters [14], [20]. Therefore, the accurate number of effective patterns can only be determined by experimental tests.

## III. Extension of the Generic Multi-frequency Model for Type 3 WTs

The generic multi-frequency modelling method is only intended for converter-connected systems such as Type 4 WTs in [14]. Based on the explanations in Part II, the RSD coupling patterns and RSD emissions are specific characteristics of Type 3 WTs, which should be addressed. In this way, the generic multi-frequency model in (1) can be extended to include the RSD couplings for Type 3 WTs. Therefore, in the coupling identification stage, the patterns related to the RSD couplings

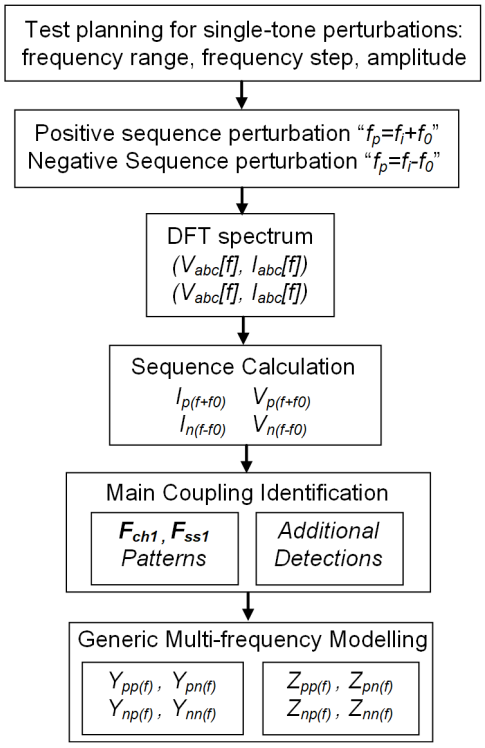


Fig. 2: Flowchart of the test procedure for the generic multi-frequency modelling.

should be included in the models. Accordingly, the generic model for Type 3 WTs can be expressed as:

$$I_{p(f_i+f_0)} = I_{p0(f_i+f_0)} + Y_{pp(f_i,f_j)}V_{p(f_i+f_0,f_j+f_0)} + Y_{pn(f_i,f_j)}V_{n(f_i+f_0,f_j-f_0)} \quad (14)$$

$$I_{n(f_i-f_0)} = I_{n0(f_i-f_0)} + Y_{np(f_i,f_j)}V_{p(f_i-f_0,f_j+f_0)} + Y_{nn(f_i,f_j)}V_{n(f_i-f_0,f_j-f_0)} \quad (15)$$

$$f_j = \begin{cases} \pm mf_i \pm kf_0, & \text{if is not RSD} \\ \pm mf_i \pm (kf_0 \pm zsf_0), & \text{if is RSD} \end{cases} \quad (16)$$

where z=1,2,... for RSD couplings. Note that the components in (14)-(15) are in matrix forms for a range of frequencies and the number of arrays depends on the number of considerable couplings in the Type 3 WT, i.,e., $f_j$. Therefore, $I_{p0}$ and $I_{n0}$ indicate the initial current emission matrices. Furthermore, $Y_{pp}$ represents the equivalent positive sequence admittance matrix among positive sequence voltages and currents, which consist of self admittance ($Y_{pp(f_i,fi)}$) as well as coupling admittance in positive sequence ($Y_{pp(f_i+f_0,fj+f_0)}, i \neq j$). $Y_{pn}$ matrix refers to the coupling admittance among positive sequence currents and negative sequence voltages, which includes the corresponding Mirror Frequency Couplings (MFC) of $Y_{pp}$ (i.e., similar patterns with $2f0$ frequency shifts in the opposite sequence [14])). Similarly, $Y_{nn}$ indicate the couplings in the negative sequence, where $Y_{nn((f_i,fi)}$ depicts the self-admittance in the negative sequence, and $Y_{nn((f_i,fj)}$ are the rest of the potential couplings in the negative sequence. Furthermore, $Y_{np}$ includes the corresponding MFCs of $Y_{nn}$.

The procedure of the generic multi-frequency modelling is illustrated in Fig. 2. Accordingly, the parameters of the generic model can be derived using single-tone positive and negative sequence perturbations as explained in [14]-[15]. In the next step, the Discrete Fourier Transform (DFT) of the WT response against perturbations are calculated and transformed to the sequence domain. Later on, a minimum noise level is used to eliminate noise and very small coupling components [14]. Moreover, the proposed coupling patterns in (8)-(9) are used to identify the main couplings and develop a generic multi-frequency model for the tested WT.

## IV. Experimental Verification of generic multi-frequency modelling for Type 3 WTs

The experimental single-tone voltage perturbation tests are performed by a 7MW/ 13.8kV/ 60Hz grid emulator at National Renewable Energy Laboratory (NREL) test site, Golden, USA [21]. The perturbation tests are performed in positive and negative sequences (with 0.01pu amplitudes) on a 2MW Type 3 WT and the WT response are measured at the POC (i.e., $V_{poc}, I_{poc}$ in Fig. 1-(a)) in steady-state conditions. The rotor slip is fixed at "s=0.175" by a torque emulator. The three-phase voltage and currents are measured using data acquisition modules with 50kS/s speed and 24bit resolution [21]. The frequency spectrum of the measured data is calculated by DFT with a 1-second frame window to achieve 1Hz resolution according to IEC 61400-4-7 [22]. The DFT results are illustrated for up to 5kHz and up to 1kHz frequency ranges to assess both high frequency and low-frequency couplings as follows:

### *A. General illustration of the DFT spectrum up to 5kHz for positive and negative perturbations*

In this case study, a group of single-tone perturbation tests is performed for the positive and negative sequences from 3Hz up to 1kHz. The DFT of the experimental results is given in Fig. 3. The frequency components in currents with amplitudes below $60\times10^{-6}$ and in voltages below $30\times10^{-6}$ are omitted to focus on the considerable components. Accordingly, the $f_p$-axis determines the frequency of single-tone voltage perturbations, $f_h$-axis illustrates the frequency of the resulting frequency components at the POC. Furthermore, the amplitudes of the corresponding DFT calculations are demonstrated with a color bar. $\{V_{p(p)}, I_{p(p)}, V_{n(p)}, I_{n(p)}\}$ (Fig. 3-a,b,c,d) refer to the DFT calculations for positive sequence voltage perturbation tests, and $\{V_{p(n)}, I_{p(n)}, V_{n(n)}, I_{n(n)}\}$ (Fig. 3-e,f,g,h) stand for the results of negative sequence voltage perturbations. Note that the perturbations have been performed for a limited number of frequencies in the range of 3Hz to 1kHz. Thus, the $f_p$-axis is discrete in the illustrated plots.

In Fig. 3, the parallel lines with $f_p$-axis represent the group of frequency components that are independent of the perturbation frequency. Therefore, these lines depict the initial emissions resulting from non-ideal converter switching and generator windings. The rest of the lines and frequency components reveal the frequency and sequence couplings in the overall WT due to perturbations. The considerable couplings

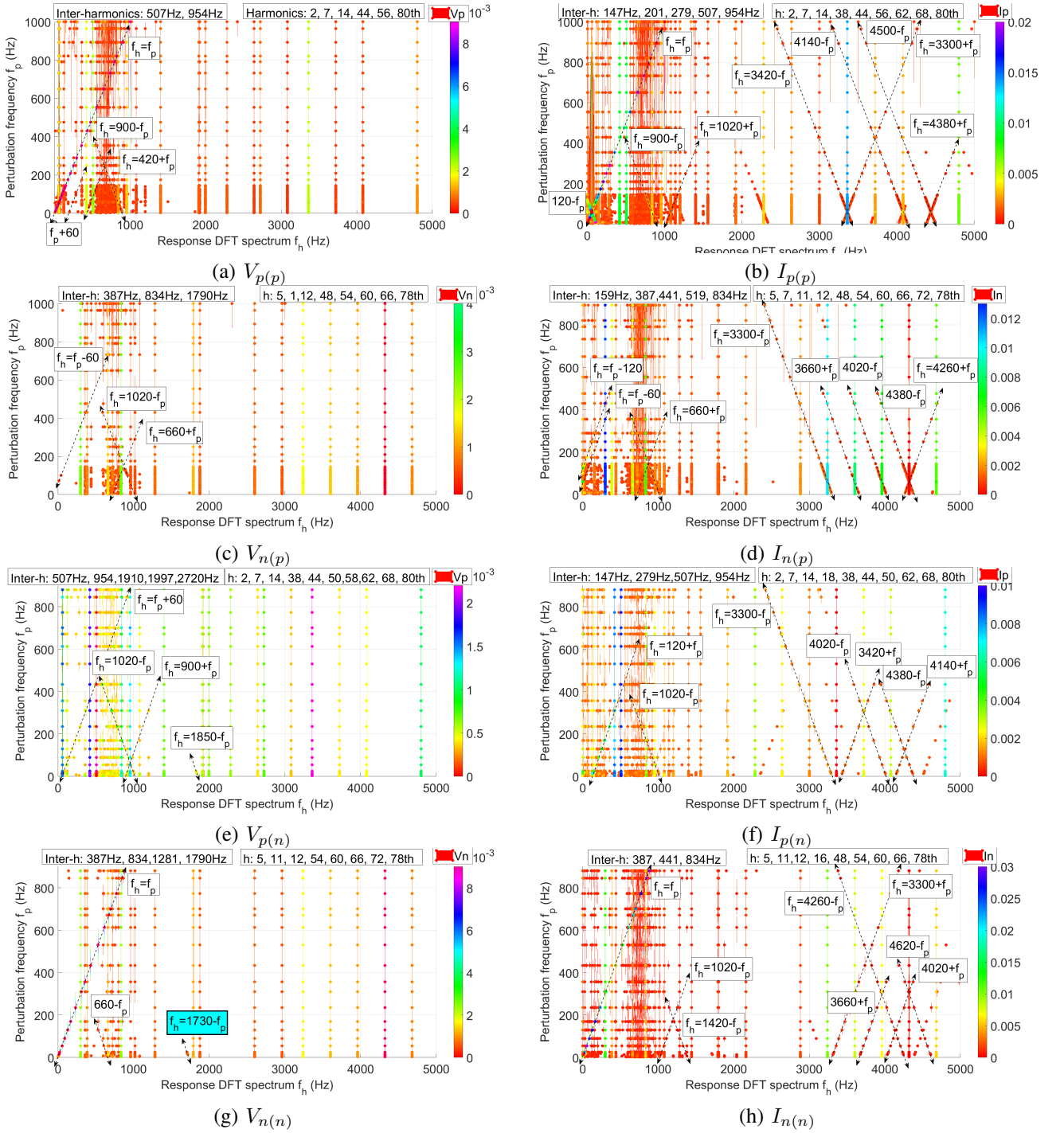


Fig. 3: DFT spectrum of voltages and currents (up to 5kHz) for experimental positive and negative sequence voltage perturbations on a 2MVA Type 3 WT (Voltage components above $30 \times 10^{-6}$ and current components above $60 \times 10^{-6}$).

are highlighted using double-edge arrows and the emissions and coupling patterns are depicted on the plots. Accordingly, a group of coupling patterns is observed in currents within the range of converters' switching frequency (3.3kHz to 4.5kHz), which are summarized in Table I. Note that the couplings are observed around the considerable emissions. This is because the root cause of the couplings is the interaction of the considerable emissions with perturbations. These couplings are mostly similar to the findings from the tests on a PV converter in [14]. In Fig. 3-(e), the only visible RSD coupling pattern is "$f_h = 1730 - f_i$". This pattern is predicted in (8) as "$f_h = -(f_p - [mf_0 - nsf_0)])$", where $f_0 = 60Hz$, m=29, n=1 and s=0.175. The negative sign is because $f_p < 1730Hz$. Note that the DFT is calculated with 1Hz resolution, thus the non-integer frequencies are presented with an accuracy of 1Hz. For instance, the given coefficients for the above-mentioned pattern leads to "$f_h = 1729.5 - f_i$", but since the resolution is 1Hz, it has been detected as "$f_h = 1730 - f_i$".

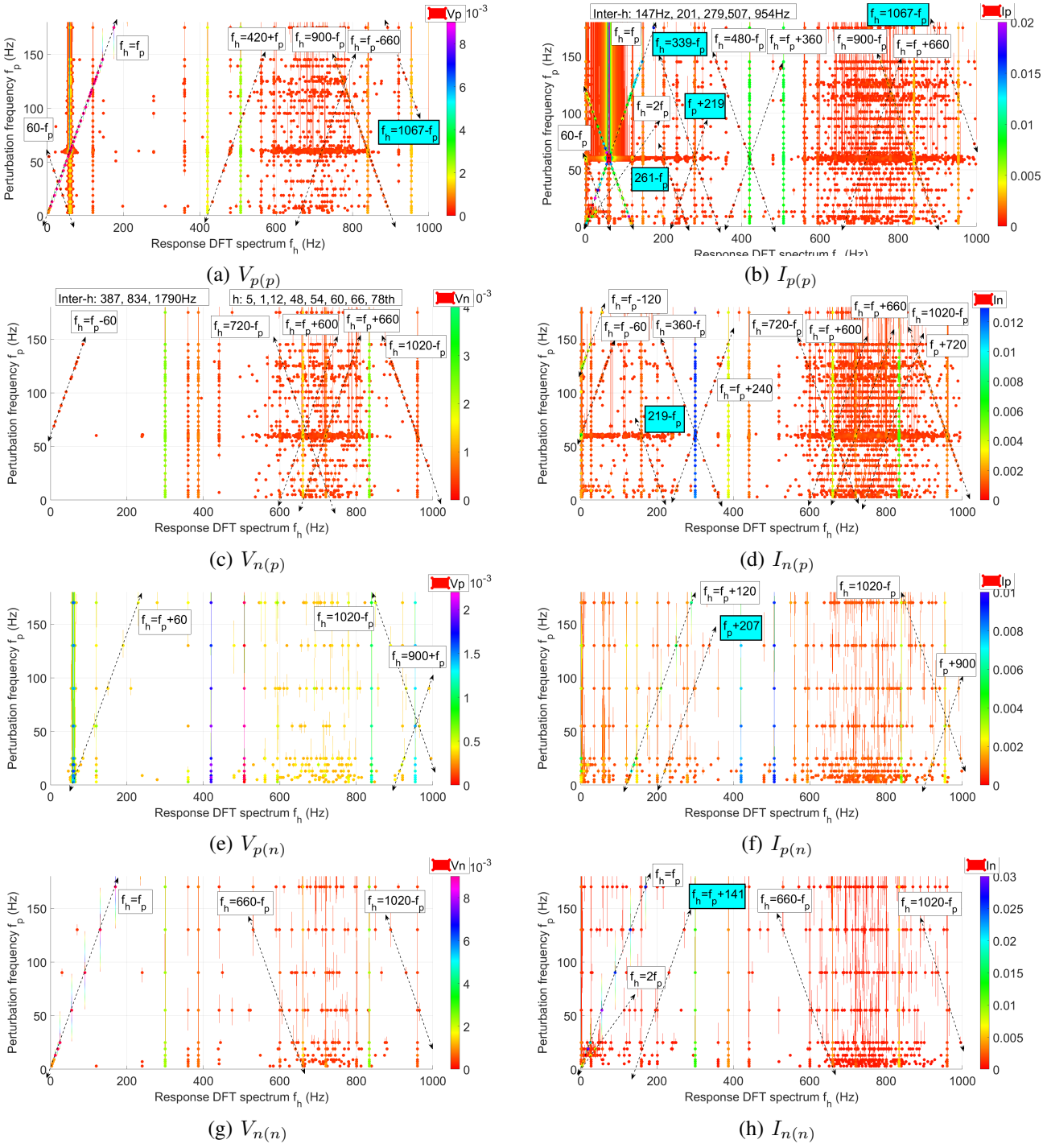


(a) $V_{p(p)}$ (b) $I_{p(p)}$ (c) $V_{n(p)}$ (d) $I_{n(p)}$ (e) $V_{p(n)}$ (f) $I_{p(n)}$ (g) $V_{n(n)}$ (h) $I_{n(n)}$

Fig. 4: Detailed DFT spectrum (up to 1kHz) for experimental perturbations below 180Hz on a 2MVA Type 3 WT.

The considerable initial emission lines, including harmonics (i.e., integer multiples of the fundamental frequency) and inter-harmonics (i.e., non-integer multiples of the fundamental frequency), are depicted in Fig. 3. The inter-harmonics refer to the RSD emissions with the patterns given in (8)-(9). For instance, in Fig. 3-(a), the RSD emissions comply with pattern "$(mf_0 \pm nsf_0)$" where s=0.175, and (m=9, n=3) for 507Hz and (m=17, n=6) for 954Hz. Furthermore, the 387Hz and 834Hz inter-harmonics are "-120Hz" shifted corresponding emissions of 507Hz and 954Hz, respectively. Such inter-harmonics can be interpreted as harmonics of "$sf_0$" along with their corresponding emissions which is called "corresponding Mirror Frequency Emissions (MFE)" in this paper. Details of the couplings for low-frequency range are not visible in Fig. 3. Therefore, more detailed plots are provided in the next section.

### *B. Detailed demonstration of DFT spectrum up to 1kHz for perturbations in low-frequency range*

The DFT spectrum of the positive and negative sequence perturbations below 180Hz are illustrated in Fig. 4. Accord-

TABLE I: Summary of the observed couplings with the positive and negative perturbations in currents ($f_0 = 60Hz$,s=0.175).

| Pattern | $I_{p(p)}$, $V_{p(p)}$ | $I_{n(n)}$, $V_{n(n)}$ |
|---|---|---|
| RSD coupling | 1067-f$_p$ $= (18f_0 - 7sf_0) - f_p, 339 - f_p = (6f_0 - 2sf_0) - f_p, 261 - f_p = (4f_0 + 2sf_0) - f_p, f_p + 219 = f_p + (4f_0 - 2sf_0)$ | 1730-f$_p$ $= (29f_0 - sf_0) - f_p, 1420 - f_p = (24f_0 - 2sf_0) - f_p, f_p + 141 = f_p + (2f_0 + 2sf_0)$ |
| RSD emission | 954Hz=(17f$_0$ $- 6sf_0), 507Hz = (9f_0 - 3sf_0), 279Hz = (5f_0 - 2sf_0), 201Hz = (3f_0 + 2sf_0), 147Hz = (3f_0 - 3sf_0)$ | 834Hz=(15f$_0$ $- 6sf_0), 442Hz = (7f_0 + 2sf_0), 387Hz = (7f_0 - 3sf_0), 159Hz = (3f_0 - 2sf_0), 27Hz = (f_0 - 3sf_0)$ |
| Harmonic coupling | 2f$_p$, $2f_0 - f_p (for f_p < 2f_0), f_0 - f_p (for f_p < f_0), f_p + f_0, f_p + 6f_0, 8f_0 - f_p, f_p + 11f_0, 15f_0 - f_p, f_p + 17f_0, 19f_0 - f_p, f_p + 55f_0, 57f_0 - f_p, 69f_0 - f_p, f_p + 73f_0, 75f_0 - f_p$ | 2f$_p$, $11f_0 - f_p, 17f_0 - f_p, f_p + 55f_0, 61f_0 - f_p, f_p + 67f_0, 71f_0 - f_p, f_p + 73f_0, 77f_0 - f_p$ |

ingly, the DFT calculations are given for up to 1kHz. Similar to Fig. 3, $f_p$-axis refers to the voltage perturbation frequency, and $f_i$-axis gives the DFT of the WT response at POC (voltage or current) with 1Hz resolution. To emphasize on the considerable components, the frequency components in currents with amplitudes below $60\times10^{-6}$ and in voltages below $30\times10^{-6}$ are neglected. The observed couplings, RSD couplings, and RSD emissions for positive sequence perturbations are summarized in Table I. The plots in Fig. 4 can be explained as follows:

*1) $V_{p(p)}$,$I_{p(p)}$:* According to Fig. 4.(a)-(b), the self-frequency excitation components have relatively high amplitudes ($f_h = f_p$ lines). As shown in Fig. 4-(b), several RSD couplings are detected in the positive sequence output current as $F_{ch(rsd)} = \{1067 - f_p, 339 - f_p, f_p + 219, 261 - f_p\}$, and their root cause emissions are $F_{em(rsd)} = \{1007Hz, 279Hz, 159Hz, 201Hz\}$ respectively. However, the RSD emissions at "1007Hz" are very small and not visible.

Furthermore, the patterns of couplings with integer harmonics are observed as: $F_{ch(h)} = \{900 - f_p, 480 - f_p, f_p + 660, f_p + 420, f_p + 360\}$. Besides, the pattern "$f_h = 2f_p$" in low frequency range for current response has not been predicted in (8)-(9), and can be considered as a design specific coupling.

*2) $V_{n(p)}$,$I_{n(p)}$:* In Fig. 4-(d), the RSD coupling pattern "$f_h = 219 - f_p$" is highlighted which is the corresponding MFC of "$f_h = 339 - f_p$" in Fig. 4-(b). Moreover, the harmonic coupling are depicted with double-arrow lines and included in Table I as: $F_{ch(h)} = \{720 \mp f_p, f_p + 660, f_p + 600, 360 - f_p, f_p + 240, f_p - 120, f_p - 60\}$. Note that "$f_h = f_p - 120$" in negative sequence is the main MFC pattern for "$f_h = f_p$" in positive sequence. The corresponding MFC concept is valid among couplings in positive (e.g., $f_h = 900 - f_p$) and negative (e.g., $f_h = 720 - f_p$) sequences.

*3) $V_{p(n)}$,$I_{p(n)}$:* Fig. 4-(e)-(f)-(g)-(h) demonstrates the results for negative sequence perturbations. The negative sequence perturbations have "$-2f_0$" frequency shift from the positive sequence perturbations. As we have explained in [14], the mirror frequency perturbations for $f_h < 120Hz$ are realized in the positive sequence, and for $f_h > 120Hz$ the experiments are conducted in the negative sequence. As shown in Fig. 4-(f), an RSD coupling is observed in the current response in the form of $F_{ch(rsd)} = \{f_p + 207\}$. Note that the $f_h = f_p + 120$ in the positive sequence is the MFC caused by negative sequence perturbation.

*4) $V_{n(n)}$,$I_{n(n)}$:* The self-frequency excitation lines ($f_h = f_p$) are illustrated in Fig. 4.(g)-(h). In addition, an RSD coupling is visible in the current response in the form of $F_{ch(rsd)} = \{f_p + 141\}$. Besides, similar to Fig 3-(b), the design specific pattern $f_h = 2f_p$ is visible in Fig. 4-(h). Note that the couplings observed for negative perturbations should be merged with the couplings for positive sequence perturbations as the patterns are similar with "$2f_0$" frequency shift.

### C. Summary of the findings

1) The amplitude of the current response can be up to 0.05 pu for 0.01pu perturbations below 200Hz, while it is small for higher frequencies.

2) Using minimum noise levels of $60\times10^{-6}$ for currents and $30\times10^{-6}$ for voltages has been effective in the detection of important couplings and emissions.

3) The observed harmonic couplings, RSD couplings, and the corresponding MFCs for positive sequence perturbations are summarized in Table I. Accordingly, the observed RSD couplings for the Type 3 WT are in general forms of "$\pm mf_i \pm kf_0 \pm zsf_0$" (m,k=0,1,2,..., and z=1,2,...), which mostly have been predicted in (8)-(9). Nevertheless, there are a few couplings that can be considered as design-specific couplings (e.g. $f_h = 2f_p$).

The RSD couplings are mostly observed in the limited range of perturbation frequencies ($f_p < 180Hz$) and response frequencies ($f_h < 1kHz$). Besides, a group of harmonic couplings is detected within the switching frequency of converters (i.e., 3.5kHz to 4.5kHz). To address the couplings in a generic model as (14)-(16), the considerable patterns should be reformulated based on $f_p$ as:

$$\begin{aligned} f_{p(p)} = \{&f_h, f_0 - f_h, f_h - f_0, f_h/2, f_h - 6f_0, 8f_0 \\ &- f_h, 15f_0 - f_h, 19f_0 - f_h, 57f_0 - f_h, f_h - 55f_0, \\ &75f_0 - f_h, f_h - 73f_0, f_h - (4f_0 - 2sf_0), (4f_0 + 2sf_0) \\ &- f_h, (6f_0 - 2sf_0) - f_h, (18f_0 - 7sf_0) - f_h\} \end{aligned} \quad (17)$$

$$f_{p(n)} = \{f_h + 2f_0, f_h + f_0, (f_h + 2f_0)/2, f_h - 4f_0, 6f_0 - f_h, 13f_0 - f_h, 17f_0 - f_h, 55f_0 - f_h, f_h - 53f_0, 73f_0 - f_h, f_h - 71f_0, f_h - (2f_0 - 2sf_0), (2f_0 + 2sf_0) - f_h, (4f_0 - 2sf_0) - f_h, (16f_0 - 7sf_0) - f_h\} \quad (18)$$

Later on, using (14)-(16) and (17)-(18), the generic multi-frequency model for the tested Type 3 WT can be developed as in (19). Accordingly, 14 couplings are included in the Norton model in this case, in which four of them are RSD couplings. The patterns in the negative sequence are corresponding MFC of positive sequence patterns. Furthermore, the coupling patterns for higher frequencies (e.g. $18f_0 - f_i$) are only effective for high-frequency ranges.

$$\begin{bmatrix} \Delta I_{p(f_i+f_0)} \\ \Delta I_{n(f_i-f_0)} \end{bmatrix} = \begin{bmatrix} Y_{pp} & Y_{pn} \\ Y_{np} & Y_{nn} \end{bmatrix} \begin{bmatrix} \Delta V_{p(f_i+f_0)} \\ \Delta V_{p(f_i)} \\ \Delta V_{p((f_i+f_0)/2)} \\ \Delta V_{p(f_i-5f_0))} \\ \Delta V_{p(7f_0-f_i)} \\ \Delta V_{p(14f_0-f_i)} \\ \Delta V_{p(18f_0-f_i)} \\ \Delta V_{p(56f_0-f_i)} \\ \Delta V_{p(f_i-54f_0)} \\ \Delta V_{p(74f_0-f_i)} \\ \Delta V_{p(f_i-72f_0)} \\ \Delta V_{p(f_i-(3f_0-2sf_0))} \\ \Delta V_{p((3f_0+2sf_0)-f_i)} \\ \Delta V_{p((5f_0-2sf_0)-f_i)} \\ \Delta V_{p((17f_0-7sf_0)-f_i)} \\ \Delta V_{n(f_i+3f_0)} \\ \Delta V_{n(f_i+2f_0)} \\ \Delta V_{n((f_i+3f_0)/2)} \\ \Delta V_{n(f_i-3f_0))} \\ \Delta V_{n(5f_0-f_i)} \\ \Delta V_{n(12f_0-f_i)} \\ \Delta V_{n(16f_0-f_i)} \\ \Delta V_{n(54f_0-f_i)} \\ \Delta V_{n(f_i-52f_0)} \\ \Delta V_{n(72f_0-f_i)} \\ \Delta V_{n(f_i-70f_0)} \\ \Delta V_{n(f_i-(f_0-2sf_0))} \\ \Delta V_{n((f_0+2sf_0)-f_i)} \\ \Delta V_{n((3f_0-2sf_0)-f_i)} \\ \Delta V_{n((15f_0-7sf_0)-f_i)} \end{bmatrix} \quad (19)$$

4) Note that the couplings observed for negative perturbations are merged with the couplings for positive sequence perturbations as the patterns are similar with "$2f_0$" frequency shift. Therefore, in a balanced system, the coupling patterns can be detected only using positive sequence perturbations. However, the negative sequence perturbations are required for the quantification of the patterns in the negative sequence.

5) According to Table I, the RSD couplings in the positive sequence have "-$2f_0$" frequency shift with the RSD couplings in the negative sequence. This finding proves that the corresponding MFC concept is valid for RSD couplings as well.

6) As shown in Fig. 4, the amplitudes of the RSD couplings are within the same range as the rest of the couplings. This means that the RSD couplings possess the same level of importance on the generic model.

7) According to Table I and the example generic model in (19), the complete extraction of the admittance vectors would require perturbation tests with high resolution such as 1 Hz resolution. Furthermore, to include the couplings with a division operand, e.g., "$(f_i + f_0)/2$" pattern in $Y_{pp}$ and "$(f_i + 3f_0)/2$" pattern in $Y_{pn}$, the perturbations with 0.5 Hz would be required. Note that this has been kept for future works because a limited number of experimental data has been accessible for this study. Nevertheless, the data has been sufficient for the detection of coupling patterns.

8) There is no considerable sequence coupling in the observations. This fact confirms that the tests are performed on a balanced system.

## V. Conclusion

The generic multi-frequency modelling method has been introduced to eliminate the need for extensive design details for multi-frequency modelling of converter-based systems. However, the Rotor-Speed Dependent (RSD) couplings and emissions in Type 3 WTs have been overlooked in the generic model. This paper extended the application of the generic multi-frequency modelling method for Type 3 WTs. Accordingly, a general theory for the RSD couplings in Type 3 WTs is introduced. The RSD couplings theory is verified by experimental perturbations on a 2MVA Type 3 WT using a 7MVA grid emulator as a perturbed AC grid and a torque emulator to fix the generator's rotor speed on a predefined value. The main frequency components including small-signal couplings, characteristic harmonic couplings, RSD couplings, and RSD emissions are identified and addressed in an example generic model. A limited number of RSD couplings are observed mainly in low-frequency range (less than 1kHz) along with corresponding MFCs. This is promising for the practical application of the proposed generic model for Type 3 WTs. Besides, the patterns of frequency and sequence couplings in converter-based systems can be generalized in the forms of "$\pm mf_i \pm kf_0 \pm zsf_0$" (m,k,z=0,1,2,...), where z can be non-zero values for Type 3 WTs. This way, the accuracy of the generic multi-frequency modelling method for Type 3 WTs is improved considerably. Besides, according to the results, a limited number of perturbation tests has been sufficient to identify the main coupling patterns; however, more tests are required to extract the admittance matrices for the generic model.

The application of the proposed generic modelling method at the system level and its comparison with analytical multi-frequency models are kept for future works.

## Acknowledgment

This work was authored in part by Alliance for Sustainable Energy, LLC, the manager and operator of the National Renewable Energy Laboratory for the U.S. Department of Energy

(DOE) under Contract No. DE-AC36-08GO28308. Funding provided by the U.S. Department of Energy Office of Energy Efficiency and Renewable Energy Wind Power Technologies Office. The views expressed in the article do not necessarily represent the views of the DOE or the U.S. Government. The U.S. Government retains and the publisher, by accepting the article for publication, acknowledges that the U.S. Government retains a nonexclusive, paid-up, irrevocable, worldwide license to publish or reproduce the published form of this work or allow others to do so, for U.S. Government purposes.

## REFERENCES

[1] Ł. H. Kocewiak, I. A. Aristi, B. Gustavsen and A. Hołdyk, "Modelling of wind power plant transmission system for harmonic propagation and small-signal stability studies," in IET Renewable Power Generation, vol. 13, no. 5, pp. 717-724, 8 4 2019, doi: 10.1049/iet-rpg.2018.5077.

[2] C. Li, "Unstable operation of photovoltaic inverter from field experiences," IEEE Trans. Pow. Del., vol. 33, no. 2, pp. 1013–1015, Apr. 2018.

[3] Buchhagen, C., Rauscher, C., Menze, A., and Jung, J.: BorWin1 – First Experiences with Harmonic Interactions in Converter Dominated Grids, International ETG Congress, VDE VERLAG gmbh, 17–18 November 2015, Berlin, Germany, 2015.

[4] M. Edrah, K. L. Lo and O. Anaya-Lara, "Impacts of High Penetration of DFIG Wind Turbines on Rotor Angle Stability of Power Systems," in IEEE Transactions on Sustainable Energy, vol. 6, no. 3, pp. 759-766, July 2015, doi: 10.1109/TSTE.2015.2412176.

[5] Y. Song, E. Ebrahimzadeh and F. Blaabjerg, "Analysis of High-Frequency Resonance in DFIG-Based Offshore Wind Farm via Long Transmission Cable," in IEEE Transactions on Energy Conversion, vol. 33, no. 3, pp. 1036-1046, Sept. 2018, doi: 10.1109/TEC.2018.2794367.

[6] I. Vieto, G. Li and J. Sun, "Behavior, Modeling and Damping of a New Type of Resonance Involving Type-III Wind Turbines," 2018 IEEE 19th Workshop on Control and Modeling for Power Electronics (COMPEL), 2018, pp. 1-8, doi: 10.1109/COMPEL.2018.8460093.

[7] I. Vieto and J. Sun, "Sequence Impedance Modeling and Analysis of Type-III Wind Turbines," in IEEE Transactions on Energy Conversion, vol. 33, no. 2, pp. 537-545, June 2018, doi: 10.1109/TEC.2017.2763585.

[8] J. Hu, Y. Huang, D. Wang, H. Yuan and X. Yuan, "Modeling of Grid-Connected DFIG-Based Wind Turbines for DC-Link Voltage Stability Analysis," in IEEE Transactions on Sustainable Energy, vol. 6, no. 4, pp. 1325-1336, Oct. 2015, doi: 10.1109/TSTE.2015.2432062.

[9] Vieto, Ignacio and Sun, Jian, "Refined Small-Signal Sequence Impedance Models of Type-III Wind Turbines," IEEE Energy Conversion Congress and Exposition (ECCE), pp. 2242-2249, Sep. 2018, doi: 10.1109/ECCE.2018.8558477.

[10] B. Liu et al., "Impedance Modeling of DFIG Wind Farms With Various Rotor Speeds and Frequency Coupling," in IEEE Transactions on Circuits and Systems II: Express Briefs, vol. 68, no. 1, pp. 406-410, Jan. 2021, doi: 10.1109/TCSII.2020.2997927.

[11] Y. Xu, H. Nian, T. Wang, L. Chen and T. Zheng, "Frequency Coupling Characteristic Modeling and Stability Analysis of Doubly Fed Induction Generator," in IEEE Transactions on Energy Conversion, vol. 33, no. 3, pp. 1475-1486, Sept. 2018, doi: 10.1109/TEC.2018.2800043.

[12] Y. Zhang, C. Klabunde and M. Wolter, "Frequency-Coupled Impedance Modeling and Resonance Analysis of DFIG-Based Offshore Wind Farm With HVDC Connection," in IEEE Access, vol. 8, pp. 147880-147894, 2020, doi: 10.1109/ACCESS.2020.3015614.

[13] IEC TR 61400-21-3: 2019 – Wind energy generation systems – Part 21-3: Measurement and assessment of electrical characteristics – Wind turbine harmonic model and its application, International Electrotechnical Commission, TC 88, ICS 28.180, 2019.

[14] B. Nouri, Ł. H. Kocewiak, S. Shah, P. Koralewicz, V. Gevorgian and P. Srensen, "Generic Multi-Frequency Modelling of Converter-Connected Renewable Energy Generators Considering Frequency and Sequence Couplings," in IEEE Transactions on Energy Conversion, doi: 10.1109/TEC.2021.3101041.

[15] B. Nouri, Ł. H. Kocewiak and et al.: Test methodology for validation of multi-frequency models of renewable energy generators using small-signal perturbations. IET Renew. Power Gener. 1–13(2021). https://doi.org/10.1049/rpg2.12245

[16] C. Larose, R. Gagnon, P. Prud'Homme, M. Fecteau and M. Asmine, "Type-III Wind Power Plant Harmonic Emissions: Field Measurements and Aggregation Guidelines for Adequate Representation of Harmonics," in IEEE Transactions on Sustainable Energy, vol. 4, no. 3, pp. 797-804, July 2013, doi: 10.1109/TSTE.2013.2252209.

[17] N. Sarma, P. M. Tuohy and S. Djurović, "Modeling, Analysis, and Validation of Controller Signal Interharmonic Effects in DFIG Drives," in IEEE Transactions on Sustainable Energy, vol. 11, no. 2, pp. 713-725, April 2020, doi: 10.1109/TSTE.2019.2904113.

[18] B. Nouri, Ł. Kocewiak, T. Jersch, G. Quistorf, C. Fenselau, I. Prima, J. Lehmann, and P. Sørensen, "Experimental Analysis of Root Causes for Rotor-Speed-Dependent Emissions from Type 3 Wind Turbines," in IEEE Transactions on Power Delivery, Jan. 2022, doi: 10.1109/TPWRD.2022.3141652.

[19] S. S. Thakur, M. Odavic, and et. al. "Theoretical Harmonic Spectra of PWM Waveforms Including DC Bus Voltage Ripple—Application to a Low-Capacitance Modular Multilevel Converter," in IEEE Transactions on Power Electronics, vol. 35, no. 9, pp. 9291-9305, Sept. 2020.

[20] M. K. Bakhshizadeh, F. Blaabjerg, J. Hjerrild, X. Wang, Ł. Kocewiak and C. L. Bak, "A Numerical Matrix-Based Method for Stability and Power Quality Studies Based on Harmonic Transfer Functions," in IEEE Journal of Emerging and Selected Topics in Power Electronics, vol. 5, no. 4, pp. 1542-1552, Dec. 2017, doi: 10.1109/JESTPE.2017.2742241.

[21] S. Shah, P. Koralewicz, V. Gevorgian, H. Liu and J. Fu, "Impedance Methods for Analyzing Stability Impacts of Inverter-Based Resources: Stability Analysis Tools for Modern Power Systems," in IEEE Electrification Magazine, vol. 9, no. 1, pp. 53-65, March 2021.

[22] Electromagnetic compatibility (EMC) – Part 4-7: Testing and measurement techniques – General guide on harmonics and interharmonics measurements and instrumentation, for power supply systems and equipment connected thereto. International Electro-technical Commission, TC 77/SC 77A, 2.1 Edition, Oct. 2009.

**Behnam Nouri** (S'18-M'21) received the B.Sc. degree in Electrical Engineering from the University of Tabriz, Iran, in 2012. In 2015, he received the M.Sc. degree in Power Electronics and Electrical Machines from the University of Tehran, Iran. With a focus on generic harmonic modelling, he received the PhD degree from the Technical University of Denmark, DTU Wind Energy Department in 2021.

Currently, he is with Hitachi Energy Sweden AB as a system studies engineer. He is an official member of IEC Technical Committee 88 contributing to electrical assessment of wind energy since 2020. His research interests include renewable energy systems, power electronics and its applications, power quality and harmonics, harmonic modelling and stability of converter-based systems, and model validation and grid code compliance tests.

**Łukasz Kocewiak** (M'12–SM'16) received the BSc and MSc degrees in electrical engineering from Warsaw University of Technology in 2007 as well as the PhD degree from Aalborg University in 2012. Currently he is with Ørsted Offshore and is working as an R&D manager. He is a power system specialist within the area of design of electrical infrastructure in large offshore wind power plants.

The main direction of his research is related to harmonics, stability and nonlinear dynamics in power electronics and power systems especially focused on wind power generation units. He is the author/co-author of more than 100 publications. He is a member of various working groups / activities within Cigré, IEEE, IEC.

**Shahil Shah** (M'18-SM'21) received the B.E. degree from Government Engineering College, Gandhinagar, India, in 2006, the M.Tech. degree from the Indian Institute of Technology (IIT) Kanpur, Kanpur, India, in 2008, and the Ph.D. degree from Rensselaer Polytechnic Institute (RPI), Troy, NY, in 2018, all in Electrical Engineering. He is currently a senior engineer in the Power Systems Engineering Center of the National Renewable Energy Laboratory (NREL), Golden, CO. His research focusses on dynamic and transient stability of renewable energy systems and power systems with high levels of inverter-based resources. He is serving as an editor of the IEEE Transactions on Energy Conversion.

Shahil was the recipient of the 2018 RPI Allen B. Dumont prize, given to a doctoral "who demonstrates candidate high scholastic ability and makes substantial contribution to his/her field."

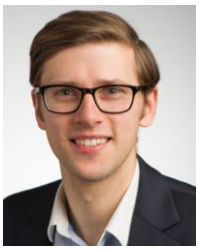

**Przemyslaw Koralewicz** (M'17) received his MSEE from Silesian Technical University in Gliwice, Poland in 2010. He specializes in modelling, detailed analysis and testing of smart inverters and complex power systems including microgrids.

He is utilizing the NREL Controllable Grid Interface (CGI), a new, groundbreaking testing apparatus and methodology to test and demonstrate many existing and future advanced controls for various renewable generation technologies on the multimegawatt scale and medium-voltage levels.

**Vahan Gevorgian** (M'97–SM'17) received the Ph.D. degree in electrical engineering from the State Engineering University of Armenia, Yerevan, Armenia, in 1993. He joined NREL in October 1994 and has served many roles over the years. He is currently working with the Power Systems Engineering Center focused on renewable energy impacts on transmission and interconnection issues and dynamic modelling of variable generation systems. He is involved in many different areas, including dynamometer and field testing of large and small wind turbines, dynamometer testing of wind turbine drive-train, development of advanced data acquisition systems, and wind turbine power quality.

Vahan provides technical support to NREL industry partners and major US wind turbine manufacturers. He is a member of the IEC team for wind turbine power quality. His contributions to NREL research have been recognized through multiple Outstanding Individual and Team Staff Awards.

**Poul Sørensen** (SM'07, F'21) is Professor in wind power integration and control in the Department of Wind Energy at the Technical University of Denmark. He was born in 1958 and received M.Sc. degree in electrical engineering from DTU in 1987. He is Convener of IEC 61400-27 electrical simulation models for wind power generation. He is also Principal Investigator and Work Package leader in several research projects and has supervised 20 PhD students and 30 Master's thesis.

He has been editor of Wiley Wind Energy 2007-13. He has been IEEE Senior Member since 2007, and he became IEEE Fellow Member in 2021 for his "contributions to wind power converter control and grid integration."